Rare Met. (2023) 42(1):76–84
https://doi.org/10.1007/s12598-022-02106-x

RARE METALS

ORIGINAL ARTICLE

Co/Zn-metal organic frameworks derived functional matrix for highly active amorphous Se stabilization and advanced lithium storage

Hong Yu, Jin-Zhao Kang, Long-Sheng Huang, Jin-Jin Wang, Xiao-Mei Wang, Xiang-Yuan Zhao, Cheng-Feng Du*

Received: 22 January 2022 / Revised: 27 April 2022 / Accepted: 9 May 2022 / Published online: 3 October 2022

Abstract Lithium–selenium batteries, as an advanced rechargeable battery system, have attracted wide attention. However, its application is hurdled by the ambiguous underlying mechanism such as the unclear active phase and the key role of the host materials. Herein, a three-dimensional (3D) functional matrix derived from the Co/Zn-metal organic framework is synthesized to unravel the questions raised. It reveals that the strong interaction and voids in the 3D matrix serve to anchor the amorphous Se with high electrochemical properties. The obtained 3DC/Se exhibits 544.2 and 273.2 $mAh \cdot g^{-1}$ at current densities of 0.1C and 2.0C, respectively, with a diffusion-controlled mechanism. The excessive amount of Se beyond the loading capacity of the matrix leads to the formation of trigonal phase Se, which shows an unsatisfying electrochemical property.

Keywords Metal–organic frameworks (MOFs); Amorphous Se; Functional matrix; Li–Se batteries

Supplementary Information The online version contains supplementary material available at https://doi.org/10.1007/s12598-022-02106-x.

H. Yu, J.-Z. Kang, L.-S. Huang, J.-J. Wang, X.-M. Wang, X.-Y. Zhao, C.-F. Du*
State Key Laboratory of Solidification Processing, Center of Advanced Lubrication and Seal Materials, Northwestern Polytechnical University, Xi'an 710072, China
e-mail: cfdu@nwpu.edu.cn

L.-S. Huang
College of Chemistry and Chemical Engineering, Hubei University, Wuhan 430062, China

C.-F. Du
Northwestern Polytechnical University Chongqing Technology Innovation Center, Chongqing 400000, China

1 Introduction

The rapid expansion of the electric vehicle industry has stimulated the demand for power sources with high energy density, and thus the development of electrochemical energy storage (EES) systems beyond the commercially available lithium-ion batteries is urgently needed [1–6]. Lithium–selenium (Li–Se) batteries, since the pioneering work of Amine's group which demonstrated the successful implementation of elemental Se in the carbonate-based electrolyte [7], have become a potential rechargeable battery system [8, 9]. Selenium (Se), as the cathode material, has a high theoretical specific capacity of 675 $mAh \cdot g^{-1}$ and a high volumetric specific capacity of 3253 $mAh \cdot cm^{-3}$ [10]. Moreover, the electrical conductivity of Se is around 1×10^{-3} $S \cdot cm^{-1}$ which exceeds that of the commercial $LiCoO_2$ cathode (1×10^{-4} $S \cdot cm^{-1}$) [3, 11]. In addition, a relatively higher melting point of Se (221 °C) than that of sulfur (112.8 °C) in the same VI A group poises it with better thermal stability and a higher endurance in the elevated working temperature [3, 12, 13]. However, Se cathode still faces problems of volume expansion during (dis)charging process, insufficient conductivity, and sluggish kinetics, leading to poor utilization and inferior performance of Se cathode [14, 15]. Therefore, the design and fabrication of an advanced Se cathode with an in-depth understanding of its underlying mechanisms is imperative to clean up the hurdles for future commercialization.

To pursue a high-performance Se cathode, much effort is contributed. It has been found that the (de)lithiation behavior and the electrochemical properties of the Se cathode are largely dependent on the form of Se [16]. Two forms of Se, i.e. the crystalline Se (trigonal phase) and the amorphous Se are reported in the literature. Generally, as compared to its crystalline counterpart, the amorphous Se cathode usually displays a better electrochemical property. Nevertheless, a different correlation between the crystallinity of Se and the phase transformation (single-phase or multi-step phase) during the lithiation process has been observed, making the working principle still ambiguous [3, 16, 17]. On the other hand, to maximize the utilization of Se cathode, a host material is usually needed which also plays a critical impact on the electrochemical performance of Se cathode [1, 18]. Many carbon-based materials have been investigated including carbon nanotubes [18, [19]], porous carbon spheres [[14], [20]], reduced graphene oxide [21], ordered mesoporous carbon [22], etc. Specifically, these porous carbon materials are able to effectively alleviate the volume expansion during the reaction process and the different pore structure is conducive to the penetration of electrolyte, thereby ensuring rapid charge transfer during cycling [23]. More importantly, these carbon host serves as a matrix to accommodate the metastable amorphous Se with abundant dangling bonds and a high surface-bulk ratio [16]. Among them, the metal–organic framework (MOF) derived functional porous carbon matrix has received wide attention attributed to the tunable metal ion/coordination ligand systems, controllable structures and adjustable pore sizes [24–27]. Various MOF-derived functional architectures have been constructed with promising applications in a variety of applications [28–31]. However, less attention is paid to the impact of the synthetic conditions of MOF-derived functional matrix on the form Se and the respective lithium-ion storage mechanism.

Therefore, we propose that a multifunctional three-dimensional (3D) porous Se matrix (3DC) can be obtained by self-assembly of Co/Zn-MOF on the tissue paper-derived carbon fibers with subsequent carbonization and Se melt-diffusion process. The obtained 3DC with rich dangling bonds and pores created by Zn evaporation acts as the perfect substrate for amorphous Se with high electrochemical capacity. Specifically, discharge specific capacities of 544.2 and 273.2 $mAh \cdot g^{-1}$ are exhibited by 3DC/Se at 0.1C and 2.0C, respectively. The electrochemical study shows the activation process of 3DC/Se in the first cycle, which is capable of decreasing the charge transfer resistance. The 3DC/Se reveals a diffusion-controlled mechanism and the capacitive contribution increases along with the scan rates. The importance of the functional 3DC matrix is investigated by varying the synthetic time and Se loading ratio. It is revealed that the increase of the thickness of the nanosheets for Co/Zn-MOF leads to a higher capability of Se loading. When an excessive amount of Se is loaded, it settles in a crystalline trigonal phase, which would deteriorate the electrochemical property.

2 Experimental

2.1 Materials preparation

Dissolving 1 mmol $Co(NO_3)_2$ and $Zn(NO_3)_2$ each into 40 ml of deionized (DI) water, which was denoted as Solution A. Afterwards, 16 mmol 2-methylimidazole was added to the same amount of DI water and recorded as Solution B. Solution A was slowly added to Solution B under stirring and then after stirring for 5 min, a clean tissue paper was immersed. The above solution was kept stationary at room temperature for 3 or 6 h before washing with DI water 3 times and drying at 60 °C overnight to obtain the Co/Zn-MOF. Finally, the as-prepared samples were heated to 800 °C for 2 h (5 $°C \cdot min^{-1}$) in a tube furnace under Ar atmosphere to obtain the 3DC matrix. The selenium is incorporated by a melt-diffusion method. Firstly, the prepared material is mixed with selenium powder in weight ratios of 50%: 50%, 40%: 60% and 30%: 70%. After grinding, the samples were put into clean quartz tubes, and the tubes were sealed in a vacuum state. Then, the quartz tubes were put into a muffle furnace and kept at 300 °C for 15 h. The samples are collected from the quartz tube after completely cooling down.

2.2 Materials characterization

A Bruker D8 advance powder diffractometer was employed to perform the powder X-ray diffraction (XRD) patterns by using Cu Kα radiation (λ = 0.15404 nm) with a scan rate of 5 $(°) \cdot min^{-1}$. A scanning electron microscopy (SEM, FEI) with an energy-dispersive X-ray spectroscopy (EDS) attachment was used to characterize the images and elemental mappings. Thermal gravimetric analysis (TGA) measurements were performed on a TG 209 F3 Tarsus® with a heating rate of 10 $°C \cdot min^{-1}$ in Ar atmosphere. X-ray photoelectron spectroscopy (XPS) analysis was performed on a XSAM-800 spectrometer.

2.3 Electrochemical measurements

The as-synthesized material (80 wt%), acetylene black (10 wt%), polyvinylidene fluoride (10 wt%) were ground before mixing them in the solvent of N-methyl pyrrolidinone (NMP). An aluminum foil as the current collector was coated with the above-prepared slurry before dying at 60 °C for 12 h under vacuum. Then, electrode disks were cut into a diameter of 12 mm with the active material loading being ~ 1.4 $mg \cdot cm^{-2}$. A porous polypropylene mat and Li-metal chip were utilized as the separator and counter/reference electrode, respectively. The electrolyte was a solution of 1.0 $mol \cdot L^{-1}$ $LiPF_6$ in a mixed solvent of ethylene carbonate (EC) (50 vol%) and dimethyl carbonate

(DMC) (50 vol%). An electrolyte dose of 40 μl was used for each coin cell and assembled in an Ar atmosphere glove box. Neware battery test systems were used for the evaluation. The cyclic voltammetries (CVs) and electrochemical impedance spectroscopy (EIS, 1×10^5–1×10^{-2} Hz) analysis were tested by Ivium. The voltage window applied was 0.6–3.0 V.

3 Results and discussion

Figure 1 is the schematic illustration of the Co/Zn-MOF nanosheets self-assembly on the tissue paper by coordination between Co^{2+}/Zn^{2+} with a molar ratio of 1:1 and 2-methylimidazole ligands in water. Here, growth time of 3 and 6 h for the Co/Zn-MOF nanosheets is investigated, which results in the variation in the thickness of the nanosheets assembled. After the subsequent heat treatment and carbonization process at 800 °C for 2 h, a 3D porous carbonaceous matrix with decorating Co species is obtained (3DC). The selenium (Se) is incorporated into the 3DC by a melt-diffusion process to obtain a 3D matrix of C/Se composite (3DC/Se).

Figure 2a exhibits broad peaks of XRD patterns at 26.6° in both 3DC-3h and 3DC-6h, which is ascribed to the (003) crystal plane of C (JCPDS No. 75-1612). While three more diffraction peaks at 44.2°, 51.5° and 75.9° originating from the (111) (200) and (220) crystal planes of Co metal (JCPDS No. 89-7093) are present as well. Diffraction peaks from orthorhombic $CoSe_2$ (JCPDS No. 53-0449) are observed only in 3DC/Se-3h and 3DC/Se-6h samples after Se melt-diffusion, indicating the conversion of metallic Co to $CoSe_2$ [32]. However, the diffraction peak of crystalline Se is not observed.

Raman spectroscopy offers a non-destructive method to characterize the structural information by detecting the vibration of signature bonds. The structural information of both 3DC/Se-3h and 3DC/Se-6h are compared in Fig. 2b. Characteristic peaks of D and G bands featuring the defect and stretching vibration in aromatic carbon materials, respectively, are detected for both samples [33–36]. The intensity ratio of D to G bands (I_D/I_G) is calculated to be 0.98 for 3DC/Se-3h and 1.01 for 3DC/Se-6h, which implies the formation of sp^2 hybridized aromatic carbon [37]. The structure of Se in the composites is also compared with bulk Se as well (Fig. 2c). The bulk Se depicts a trigonal phase where a characteristic peak at 237 cm^{-1} is observed, signifying the first-order A_1 symmetric stretching mode of trigonal Se [38, 39]. After being incorporated into the 3DC matrix, both 3DC/Se-3h and 3DC/Se-6h display a chain-like structure with the characteristic peak shifting to 257 cm^{-1}. This Se is amorphous with disordered Se_n chains, which experience stronger interactions with the 3DC matrix than Se–Se bonding in the trigonal phase [22, 38]. Interesting to note that, the Se form in 3DC/Se is also different from that in the literature, where Se in the form of Se_8 rings was observed in ordered mesoporous carbon (CMK-3) matrix [38, 40]. The content of Se in the 3DC matrix is measured by TGA under Ar atmosphere (Fig. S1), which is determined to be 34.8 wt% and 40.1 wt% for 3DC/Se-3h and 3DC/Se-6h, respectively. This indicates that thicker nanosheets are obtained with the increase of Co/Zn-MOF growth time, which guarantees a higher Se content.

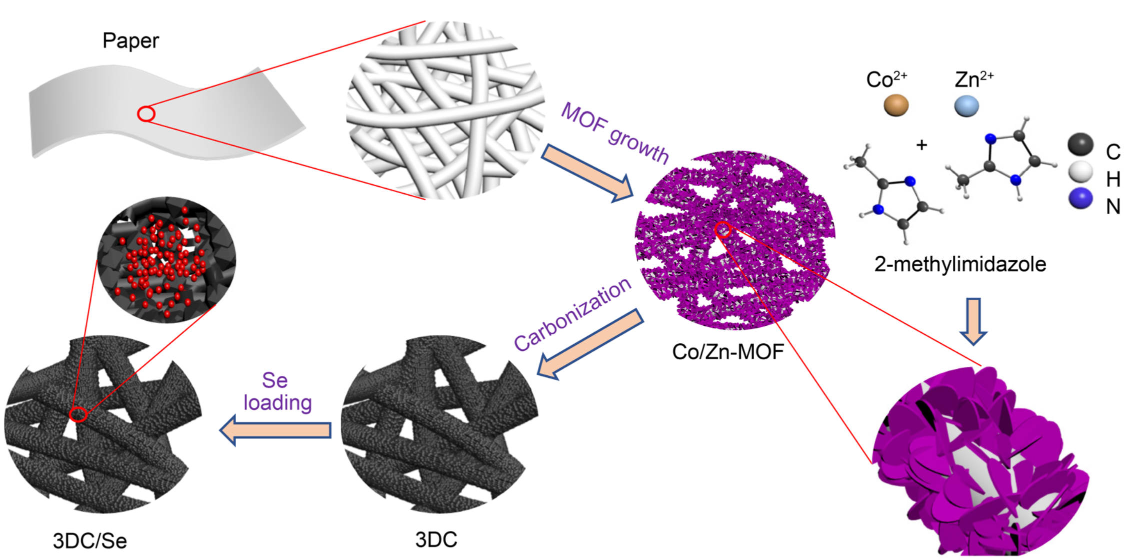

Fig. 1 Illustrated synthetic process of 3DC/Se

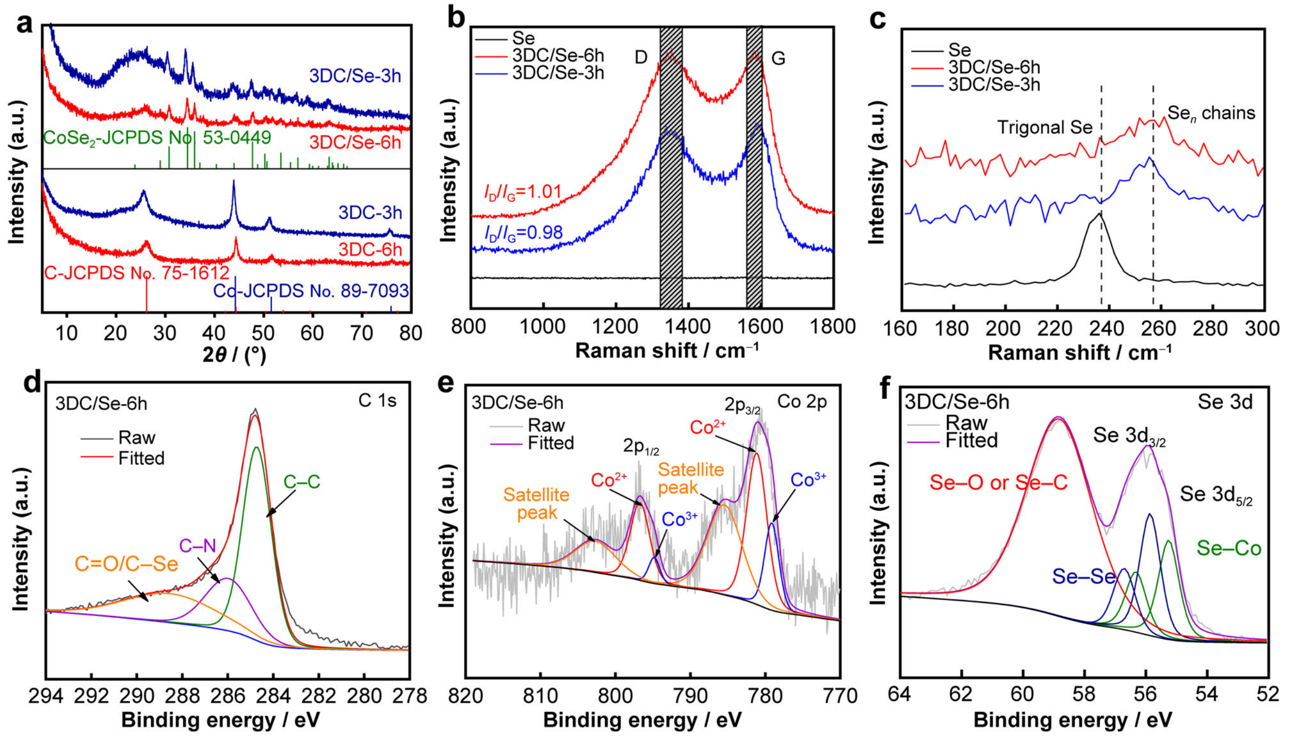

Fig. 2 **a** XRD patterns of 3DC-3h, 3DC-6h, 3DC/Se-3h, 3DC/Se-6h; **b, c** Raman spectra of Se, 3DC/Se-3h and 3DC/Se-6h; XPS spectra of 3DC/Se-6h: **d** C 1s, **e** Co 2p and **f** Se 3d

XPS are further acquired to probe the chemical state of the as-prepared 3DC/Se-6h. In the high-resolution C 1s spectrum (Fig. 2d), three peaks are deconvoluted corresponding to C–C (284.7 eV), C–N (286.0 eV) and C=O/C–Se (289.1 eV), respectively. In the Co core electron levels (Fig. 2e), Co^{2+} $2p_{1/2}/2p_{3/2}$ and Co^{3+} $2p_{1/2}/2p_{3/2}$ pairs are identified at 796.7/781.2 and 794.9/779.3 eV, respectively [1, 41–44]. Noted that no signal from Zn 2p core level in the range of 1010–1060 eV is detected, indicating the absence of Zn metal in the 3DC/Se-6h sample (Fig. S2). During the heat treatment process at 800 °C, Zn species vaporize and escape from the 3DC, leaving voids and dangling bonds in the matrix [1, 24]. Centering on the Se 3d spectrum (Fig. 2f), peaks at 56.8/56.3 and 55.8/55.3 eV are related to the $3d_{3/2}$ of Se–Se/Se–Co and $3d_{5/2}$ of Se–Se/Se–Co, respectively. The existence of the Se–Co bond proves the generation of $CoSe_2$, which is consistent with XRD results. The Se–Se bond indicates that Se is not completely converted to $CoSe_2$. Combined with XRD results, it is proved that though the existence of $CoSe_2$, a portion of Se is still in an amorphous elemental state. [32, 45, 46].

SEM is utilized to understand the morphological information of the samples. The nanosheet morphology of Co/Zn-MOF can be observed (Fig. S3). As observed in Fig. 3a, b, 3DC/Se-3h reveals a coral-like morphology interconnecting to form a 3D matrix. No big bulky structures are observed. EDS results in Fig. 3c unveil the uniform distribution of C, Se and Co in 3DC/Se-3h, indicating that Se are uniformly distributed in 3DC matrix. Similar morphology and homogeneous distribution of C, Se and Co are also uncovered in 3DC/Se-6h.

The lithium storage properties of both 3DC/Se-3h and 3DC/Se-6h samples are evaluated in a coin-type of cell with the lithium plate as the counter and reference electrode. CV scans are performed in the voltage range of 0.6–3.0 V at a scan rate of 0.1 $mV \cdot s^{-1}$. Figure 4a shows the initial five CV scans of 3DC/Se-3h. A broad cathodic peak at 1.2 V and an anodic peak at 2.2 V are observed in the first CV cycle, corresponding to the formation of Li_2Se and restoration of Se/$CoSe_2$, respectively. From the second cycle onwards, the cathodic peak shifts to 1.75 V with a shoulder peak at 1.35 V. This shifting was also observed in the previous report which is attributed to the activation of the C/Se based composite in the first cycle [1, 32]. Specifically, the redox pair at 2.10/1.35 V originates from the reversible redox reaction of $CoSe_2$ and the redox pair at 2.30/1.75 V is featured with the redox of amorphous Se [28, 32]. While the anodic peak splits into two peaks at 2.1 and 2.3 V. From the second cycle onwards, the CV curves gradually overlap with each other, revealing good reversibility of the electrode. While for 3DC/Se-6h electrode (Fig. 4b), a similar activation process in the first cycle and shifting of the redox pairs to 2.15/1.15 V are

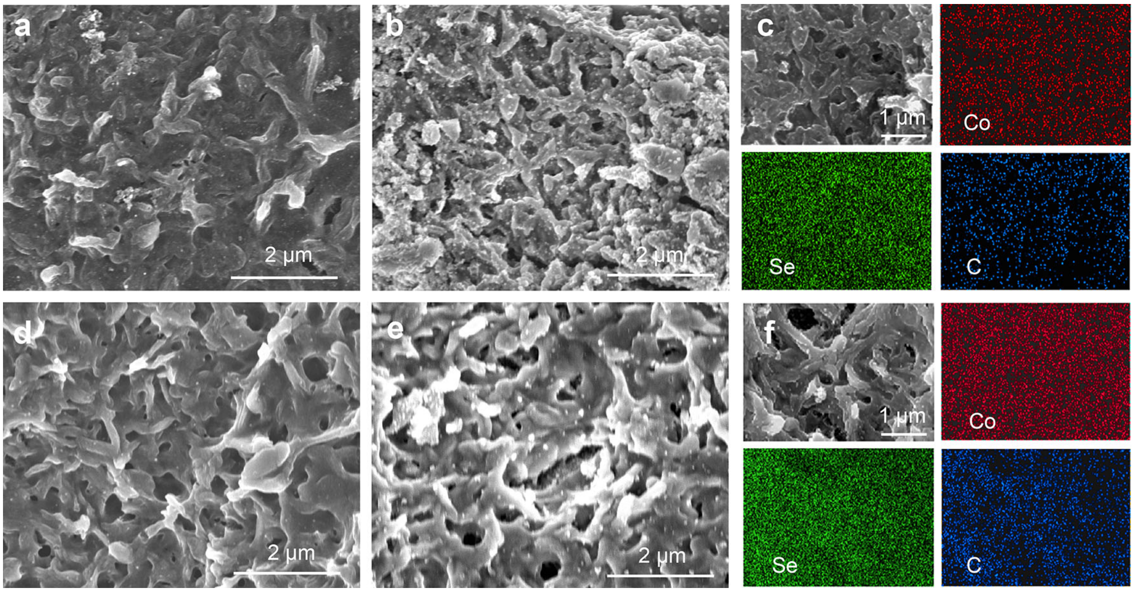

Fig. 3 **a** SEM image of 3DC-3h; **b** SEM image and **c** elemental mapping images of 3DC/Se-3h; **d** SEM image of 3DC-6h; **e** SEM image and **f** elemental mapping images of 3DC/Se-6h

uncovered. Specifically, the capacity contribution ratio from Se increases, as indicated in the relative peak ratio. Moreover, a smaller polarization is detected in 3DC/Se-6h (300 mV) than that in 3DC/Se-3h (517 mV), implying that faster kinetics can be obtained with a thicker carbon matrix.

The rate capability of 3DC/Se samples is compared in Fig. 4c. For 3DC/Se-6h, at a current density of 0.1C (1.0C = 675 mAh·g^{-1}), a discharge capacity of 544.2 mAh·g^{-1} is exhibited in the second cycle. When the current densities are increased to 0.2C, 0.5C, 1.0C and 2.0C, the second cycle discharge capacities exhibited are 413.8, 363.7, 315.5 and 273.2 mAh·g^{-1}. When the current density decreases to 0.2C, a constant discharge capacity of 359.4 mAh·g^{-1} is restored. While inferior rate capability of 3DC/Se-3h is obtained with discharge capacities of 186.9 and 150.1 mAh·g^{-1} at 1.0C and 2.0C. The corresponding galvanostatic charge–discharge (GCD) curves of 3DC/Se-6h are displayed in Fig. 4d. As observed, the redox reaction of amorphous Se is expressed as a sloping plateau at 2.1/1.8 V and a step in the discharge curve at 1.4 V attributes to the reduction of $CoSe_2$, which are consistent with the CV results. Additionally, GCD curves of 3DC/Se-3h are similar to those of 3DC/Se-6h (Fig. S4). The well-defined plateaus of 3DC/Se-6h throughout current densities from 0.1C to 2.0C imply good reversibility. The stability is tested at 1.0C (Fig. S5) with prior pre-activation at 0.1C for 3 cycles. After 1000 cycles, a specific capacity of 197.9 mAh·g^{-1} is achieved by 3DC/Se-6h (69% capacity retention related to the initial cycle), which outperforms that of 3DC/Se-3h (169.4 mAh·g^{-1}).

The charge transfer kinetics of both electrodes are studied by EIS. A considerably smaller semi-circle is plotted for 3DC/Se-6h (Fig. 4e), whose value is the indicator of the interfacial charge transfer resistance (R_{ct}). The obtained Nyquist plots with the equivalent circuit is fitted in the inset, where R_s is the resistance of the electrolyte, R_{ct1} represents the charge transfer resistance of the SEI of electrolyte and the R_{ct2} signifies the charge transfer resistance between the composite and electrolyte. In addition, it also includes Warburg resistance (Z_w) and space charge capacitance (constant phase element (CPE)). Thus, the R_{ct} of 3DC/Se-6h and 3DC/Se-3h is calculated as the sum of R_{ct1} and R_{ct2} to be 133.5 and 995.4 Ω, respectively, indicating a much-enhanced charge transfer resistance of 3DC/Se-6h [9]. After 5 cycles, decreases of R_{ct} are detected in both 3DC/Se-6h and 3DC/Se-3h electrodes (Fig. 4f), which reveals the activation of electrode material and is consistent with CV results. The respective resistance values obtained by fitting are shown in Table S1.

The electrochemical behavior of 3DC/Se electrodes is further understood by CV measurements at different scan rates of 0.1–2.0 mV·s^{-1} (Figs. 4g, S6). Generally, two types of Li^+ storage mechanisms can be classified through the relationship of peak current (i) and scan rate (v):

$$i = av^b \tag{1}$$

$$\lg i = b \lg v + \lg a \tag{2}$$

where a and b are two empirical constants [1, 34, 47]. The values of b indicate an energy storage mode, in which b = 0.5 represents a reaction of a typical diffusion-controlled process, while b = 1 for a surface capacitive-

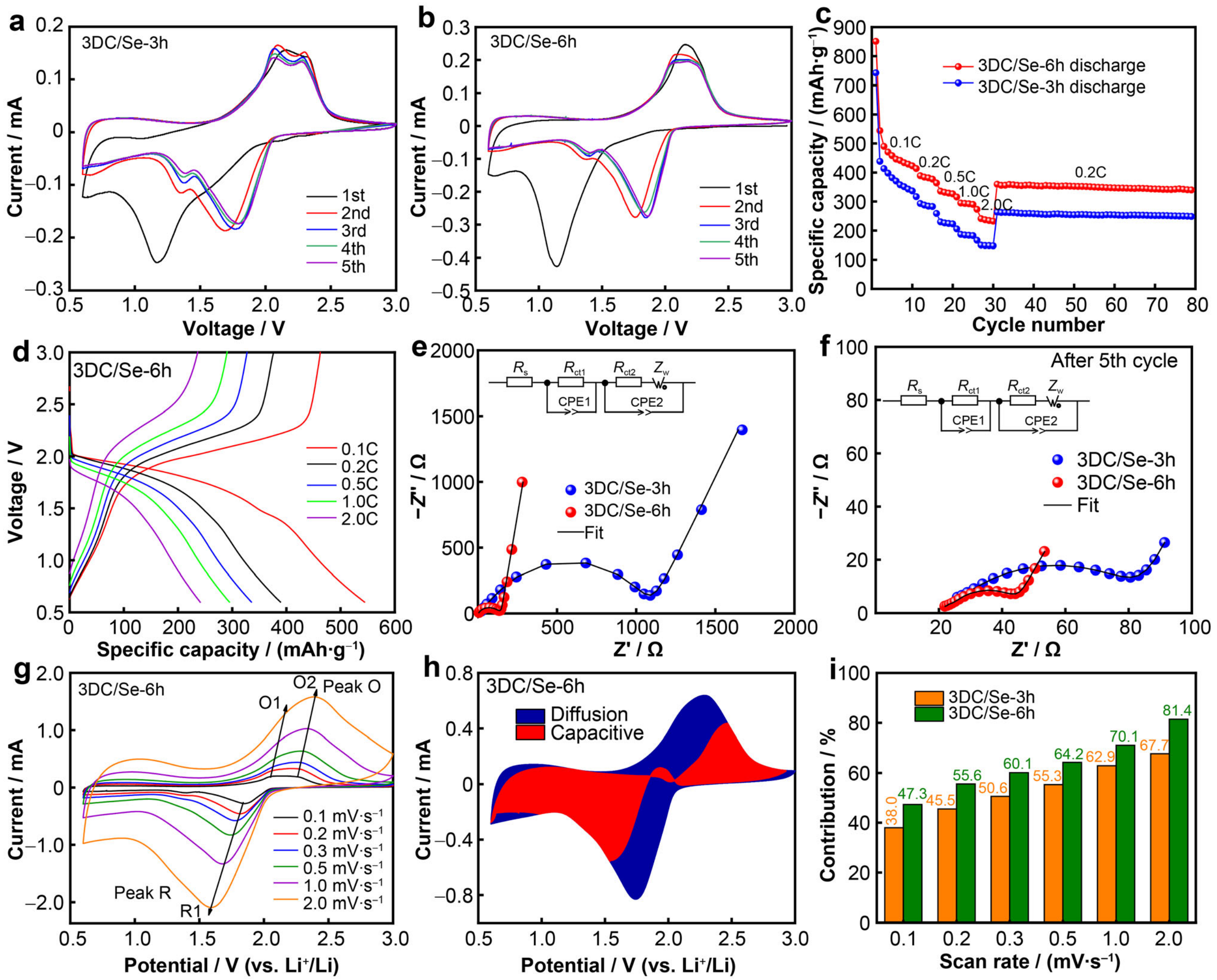

Fig. 4 CV curves (0.1 mV·s^{-1}) of **a** 3DC/Se-3h and **b** 3DC/Se-6h; **c** rate capability of 3DC/Se-3h and 3DC/Se-6h; **d** GCD curves of 3DC/Se-6h at 0.1C–2.0C; **e** Nyquist plots of 3DC/Se-3h and 3DC/Se-6h before cycling; **f** Nyquist plots of 3DC/Se-3h and 3DC/Se-6h after 5 cycles, where Z' is real part of impedance and Z'' is imaginary part of impedance; **g** CV curves of 3DC/Se-6h with different scan rates; **h** capacitive contribution (0.5 mV·s^{-1}); **i** capacitive contribution at various scan rates

controlled process. And the values of b could be obtained via linear fitting lg$i$ and lg$v$. Figure S7a shows the fitting results for 3DC/Se-6h, in which the values of b for R1, O1 and O2 peaks are 0.67, 0.56, and 0.70, respectively. The low values of b indicate that the electrochemical behavior is based on the diffusion-controlled process. Comparatively, the values of b for 3DC/Se-3h are close to those of 3DC/Se-6h, which suggests a similar charge storage mechanism (Fig. S7b). Based on the above results, the diffusion and capacitive contribution ratio is plotted in Figs. 4h, i and S8. The capacitance contributions for both samples increase with the scan rates increasing (Fig. 4i) from 47.3% to 81.4% for 3DC/Se-6h electrode, higher than those of 3DC/Se-3h electrode (38.0% to 67.7%). Therefore, 3DC/Se-6h shares a similar diffusion-controlled Li^+ storage mechanism with a larger capacitance contribution compared to the 3DC/Se-3h.

In order to further probe the correlation between the MOF-derived functional matrix (3DC) and the form of Se, Se with different amounts was incorporated into the 3DC/Se-6h matrix and the structural characteristics and electrochemical properties of the as-obtained samples were studied. The weight ratio between 3DC-6h and Se investigated are 50%: 50% named 3DC50%–Se50%, 40%: 60% named 3DC40%–Se60% and 30%: 70% named 3DC30%–Se70%. As shown in XRD results (Fig. 5a), no crystalline Se is detected in 3DC50%–Se50%. However, with the increase of Se content, both 3DC40%–Se60% and 3DC30%–Se70% samples show a crystalline Se phase (JCPDS No. 06-0362). Raman spectroscopy is also

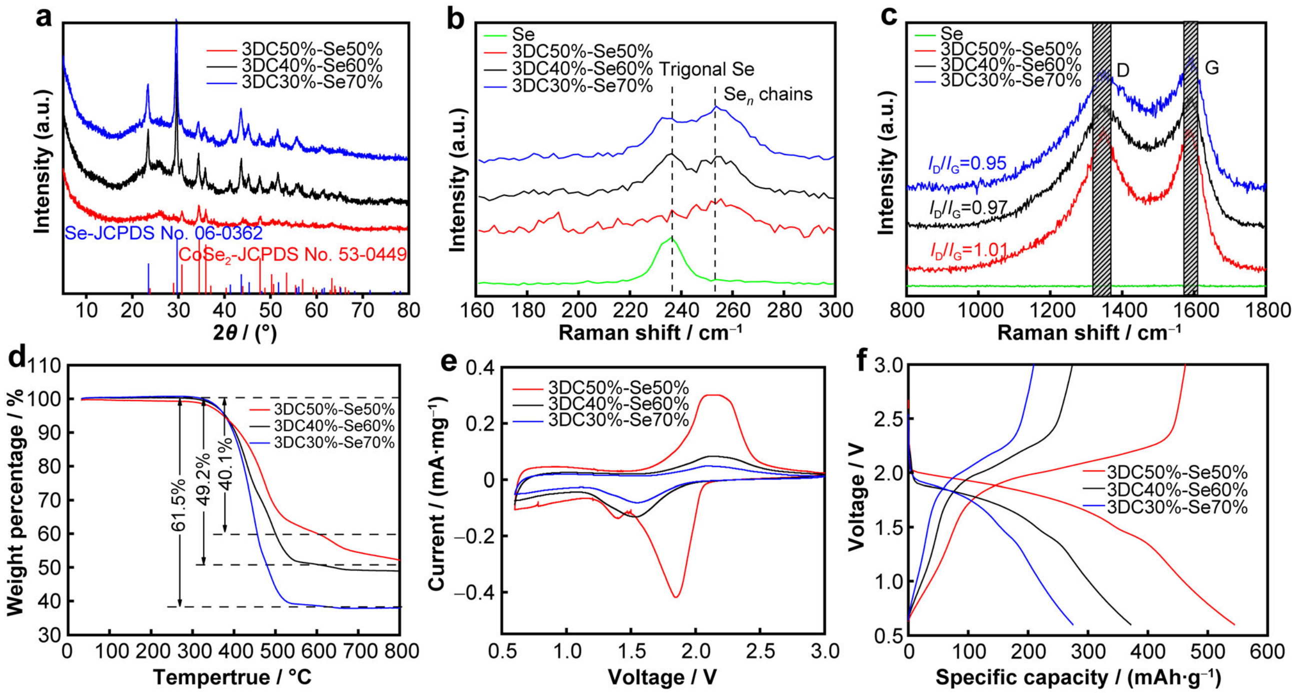

Fig. 5 **a** XRD patterns of 3DC50%–Se50%, 3DC40%–Se60% and 3DC30%–Se70%; **b, c** Raman spectra of 3DC50%–Se50%, 3DC40%–Se60% and 3DC30%–Se70%; **d** TGA curves of 3DC50%–Se50%, 3DC40%–Se60% and 3DC30%–Se70% in Ar atmosphere; **e** CV curves and **f** GCD curves of 3DC50%–Se50%, 3DC40%–Se60% and 3DC30%–Se70%

employed. In Fig. 5c, the presence of characteristic D and G bands with similar intensity ratios indicates the formation of similar sp^2 hybridized carbon materials. However, on top of the Se_n chain band at 257 cm^{-1} observed in all three samples, additional characteristic bands of trigonal Se at 237 cm^{-1} are detected for 3DC40%–Se60% and 3DC30%–Se70% while absent in 3DC50%–Se50% (Fig. 5b). The accurate contents of Se in the composite determined by TGA are 40.1%, 49.2% and 61.5% for 3DC50%–Se50%, 3DC40%–Se60% and 3DC30%–Se70%, respectively (Fig. 5d). It is therefore conjectured that the strong interaction of the 3DC matrix and Se plays an important role in stabilizing Se in an amorphous state. When the amount of Se exceeds the loading capability of 3DC matrix, Se presents in the form of a crystalline trigonal phase as bulk Se.

The electrochemical properties of 3DC/Se with different Se ratios are compared to investigate the impact of the Se crystallinity. 3DC40%–Se60% and 3DC30%–Se70% samples underwent similar activation processes on the first CV curve (Fig. S9). From the second cycle onwards, redox reactions with good reversibility and overlapping of CV curves are displayed in both samples. Nonetheless, a smaller redox area for the CV curves along with the decrease in the specific capacity is observed when the Se content increases (Fig. 5e). Moreover, a larger polarization with deteriorated kinetics is revealed with the presence of crystalline trigonal phase Se. These CV results are also consistent with GCD curves in Fig. 5d, where the lowering in specific capacity and increase in polarization are getting worse with the increase of crystalline Se. EIS curves in Fig. S10 further disclose a dramatically decreased R_{ct} of 3DC50%–Se50% compared to that of the other two, whose fitted values from the equivalent circuit are shown in Table S2. This implies that the transition of Se from amorphous to crystalline nature results in a dramatic increase of R_{ct} with insufficient kinetics, which is one of the causes of the deteriorated performances. Therefore, the high capacity of Se mainly originates from the amorphous phase, which needs to be stabilized in a matrix with strong interactions. When an excessive amount of Se is present, Se tends to form trigonal phase Se and deteriorates the electrochemical properties.

4 Conclusion

In summary, Co/Zn-MOF nanosheets are assembled on the surface of the tissue paper serving as a substrate before the subsequent carbonization to obtain a 3D porous functional matrix 3DC. The 3DC/Se composite is further obtained by a melt-diffusion method where the amorphous Se is uniformly distributed and stabilized by the strong interaction with the matrix. The 3DC/Se exhibits an activation process in the first cycle and stabilizes onwards with a decrease in the charge transfer resistance. The 3DC/Se reveals a diffusion-controlled process and the capacitive contribution increases along with the scan rates. The increase of the growth time for Co/Zn-MOF nanosheets leads to a larger thickness of the nanosheets, which further guarantees an increase in capability of Se loading. The 3DC functional matrix plays an important role in stabilizing the amorphous Se, which is also the origin of the high capacity. When the loading content of Se exceeds the capability of the matrix, crystalline trigonal phase Se forms with unsatisfying electrochemical performance.

Acknowledgements This work was financially supported by the National Natural Science Foundation of China (Nos. 51901189 and 51802265), Shaanxi Provincial Key R&D Program (No. 2021KWZ-17), China Postdoctoral Science Foundation Grant (No. 2020M683552) and the Natural Science Foundation of Chongqing (No. cstc2020jcyj-msxmX0859).

Declarations

Conflict of interests The authors declare that they have no conflict of interest.

References

[1] Tian H, Tian H, Wang S, Chen S, Zhang F, Song L, Liu H, Liu J, Wang G. High-power lithium–selenium batteries enabled by atomic cobalt electrocatalyst in hollow carbon cathode. Nat Commun. 2020;11(1):5025. https://doi.org/10.1038/s41467-020-18820-y.

[2] Wang J, Kang J, Gu ZY, Liang Q, Zhao X, Wang X, Guo R, Yu H, Du CF, Wu XL. Localized electron density redistribution in fluorophosphate cathode: dangling anion regulation and enhanced na-ion diffusivity for sodium-ion batteries. Adv Funct Mater. 2021;32(4):2109694. https://doi.org/10.1002/adfm.202109694.

[3] Sun J, Du Z, Liu Y, Ai W, Wang K, Wang T, Du H, Liu L, Huang W. State-of-the-art and future challenges in high energy lithium–selenium batteries. Adv Mater. 2021;33(10):2003845. https://doi.org/10.1002/adma.202003845.

[4] Fei R, Wang H, Wang Q, Qiu R, Tang S, Wang R, He B, Gong Y, Fan HJ. In situ hard-template synthesis of hollow bowl-like carbon: a potential versatile platform for sodium and zinc ion capacitors. Adv Energy Mater. 2020;10(47):2002741. https://doi.org/10.1002/aenm.202002741.

[5] Wang J, Du CF, Xue Y, Tan X, Kang J, Gao Y, Yu H, Yan Q. MXenes as a versatile platform for reactive surface modification and superior sodium-ion storages. Exploration. 2021;1(2):20210024. https://doi.org/10.1002/EXP.20210024.

[6] Liang HJ, Gu ZY, Zhao XX, Guo JZ, Yang JL, Li WH, Li B, Liu ZM, Li WL, Wu XL. Ether-based electrolyte chemistry towards high-voltage and long-life na-ion full batteries. Angew Chem Int Ed Engl. 2021;60(51):26837. https://doi.org/10.1002/anie.202112550.

[7] Abouimrane A, Dambournet D, Chapman KW, Chupas PJ, Weng W, Amine K. A new class of lithium and sodium rechargeable batteries based on selenium and selenium–sulfur as a positive electrode. J Am Chem Soc. 2012;134(10):4505. https://doi.org/10.1021/ja211766q.

[8] Kim S, Cho M, Lee Y. High-performance Li–Se battery enabled via a one-piece cathode design. Adv Energy Mater. 2019;10(5):1903477. https://doi.org/10.1002/aenm.201903477.

[9] Balakumar K, Kalaiselvi N. Selenium containing tube-in-tube carbon: a one dimensional carbon frame work for selenium cathode in Li–Se battery. Carbon. 2017;112:79. https://doi.org/10.1016/j.carbon.2016.10.097.

[10] Jin J, Tian X, Srikanth N, Kong LB, Zhou K. Advances and challenges of nanostructured electrodes for Li–Se batteries. J Mater Chem A. 2017;5(21):10110. https://doi.org/10.1039/C7TA01384A.

[11] Zhang F, Xiong P, Guo X, Zhang J, Yang W, Wu W, Liu H, Wang G. A nitrogen, sulphur dual-doped hierarchical porous carbon with interconnected conductive polyaniline coating for high-performance sodium–selenium batteries. Energy Stor Mater. 2019;19:251. https://doi.org/10.1016/j.ensm.2019.03.019.

[12] Dong WD, Yu WB, Xia FJ, Chen LD, Zhang YJ, Tan HG, Wu L, Hu ZY, Mohamed HSH, Liu J, Deng Z, Li Y, Chen LH, Su BL. Melamine-based polymer networks enabled N, O, S Co-doped defect-rich hierarchically porous carbon nanobelts for stable and long-cycle Li-ion and Li–Se batteries. J Colloid Interface Sci. 2021;582(A):60. https://doi.org/10.1016/j.jcis.2020.06.071.

[13] Singh A, Kalra V. Electrospun nanostructures for conversion type cathode (S, Se) based lithium and sodium batteries. J Mater Chem A. 2019;7(19):11613. https://doi.org/10.1039/C9TA00327D.

[14] Lei Z, Lei Y, Liang X, Yang L, Feng J. High stable rate cycling performances of microporous carbon spheres/selenium composite (MPCS/Se) cathode as lithium–selenium battery. J Power Sources. 2020;473:228611. https://doi.org/10.1016/j.jpowsour.2020.228611.

[15] Lu P, Liu F, Zhou F, Qin J, Shi H, Wu ZS. Lignin derived hierarchical porous carbon with extremely suppressed polyselenide shuttling for high-capacity and long-cycle-life lithium–selenium batteries. J Energy Chem. 2021;55:476. https://doi.org/10.1016/j.jechem.2020.07.022.

[16] Zhou X, Gao P, Sun S, Bao D, Wang Y, Li X, Wu T, Chen Y, Yang P. Amorphous, crystalline and crystalline/amorphous selenium nanowires and their different (de)lithiation mechanisms. Chem Mater. 2015;27(19):6730. https://doi.org/10.1021/acs.chemmater.5b02753.

[17] Cui Y, Abouimrane A, Sun CJ, Ren Y, Amine K. Li–Se battery: absence of lithium polyselenides in carbonate based electrolyte. Chem Commun (Camb). 2014;50(42):5576. https://doi.org/10.1039/C4CC00934G.

[18] Yao Y, Chen M, Xu R, Zeng S, Yang H, Ye S, Liu F, Wu X, Yu Y. CNT interwoven nitrogen and oxygen dual-doped porous carbon nanosheets as free-standing electrodes for high-performance Na-Se and K-Se flexible batteries. Adv Mater. 2018;30(49):1805234. https://doi.org/10.1002/adma.201805234.

[19] He J, Chen Y, Lv W, Wen K, Li P, Wang Z, Zhang W, Qin W, He W. Three-dimensional hierarchical graphene-CNT@Se: a highly efficient freestanding cathode for Li–Se batteries. ACS Energy Lett. 2016;1(1):16. https://doi.org/10.1021/acsenergylett.6b00015.

[20] Zhao P, Shiraz MHA, Zhu H, Liu Y, Tao L, Liu J. Hierarchically porous carbon from waste coffee grounds for high-performance Li–Se batteries. Electrochim Acta. 2019;325:134931. https://doi.org/10.1016/j.electacta.2019.134931.

[21] Peng X, Wang L, Zhang X, Gao B, Fu J, Xiao S, Huo K, Chu PK. Reduced graphene oxide encapsulated selenium nanoparticles for high-power lithium–selenium battery cathode. J Power Sources. 2015;288:214. https://doi.org/10.1016/j.jpowsour.2015.04.124.

[22] Wang X, Tan Y, Liu Z, Fan Y, Li M, Younus HA, Duan J, Deng H, Zhang S. New insight into the confinement effect of microporous carbon in Li/Se battery chemistry: a cathode with enhanced conductivity. Small. 2020;16(17):2000266. https://doi.org/10.1002/smll.202000266.

[23] Nie Z, Zhang H, Lu Y, Han C, Du Y, Sun Z, Yan Y, Yu H, Zhang X, Zhu J. Manipulation of porosity and electrochemical artificial separator interphase for durable lithium–sulfur batteries. Chem Eng J. 2021;409:128137. https://doi.org/10.1016/j.cej.2020.128137.

[24] Park SK, Park JS, Kang YC. Metal–organic-framework-derived N-doped hierarchically porous carbon polyhedrons anchored on crumpled graphene balls as efficient selenium hosts for high-performance lithium–selenium batteries. ACS Appl Mater Interface. 2018;10(19):16531. https://doi.org/10.1021/acsami.8b03104.

[25] Cao Y, Lei F, Li Y, Qiu S, Wang Y, Zhang W, Zhang Z. A MOF-derived carbon host associated with Fe and Co single atoms for Li–Se batteries. J Mater Chem A. 2021;9(29):16196. https://doi.org/10.1039/D1TA04529F.

[26] Li S, Yang H, Xu R, Jiang Y, Gong Y, Gu L, Yu Y. Selenium embedded in MOF-derived N-doped microporous carbon polyhedrons as a high performance cathode for sodium-selenium batteries. Mater Chem Front. 2018;2(8):1574. https://doi.org/10.1039/C8QM00177D.

[27] Song JP, Wu L, Dong WD, Li CF, Chen LH, Dai X, Li C, Chen H, Zou W, Yu WB, Hu ZY, Liu J, Wang HE, Li Y, Su BL. MOF-derived nitrogen-doped core-shell hierarchical porous carbon confining selenium for advanced lithium–selenium batteries. Nanoscale. 2019;11(14):6970. https://doi.org/10.1039/C9NR00924H.

[28] Hou BH, Wang YY, Liu DS, Gu ZY, Feng X, Fan HS, Zhang TF, Lu CL, Wu XL. N-doped carbon-coated $Ni_{1.8}Co_{1.2}Se_4$ nanoaggregates encapsulated in N-doped carbon nanoboxes as advanced anode with outstanding high-rate and low-temperature performance for sodium-ion half/full batteries. Adv Funct Mater. 2018;28(47):1805444. https://doi.org/10.1002/adfm.201805444.

[29] Cheng WZ, Liang JL, Yin HB, Wang YJ, Yan WF, Zhang JN. Bifunctional iron-phtalocyanine metal–organic framework catalyst for ORR, OER and rechargeable zinc–air battery. Rare Met. 2020;39(7):815. https://doi.org/10.1007/s12598-020-01440-2.

[30] Li C, Zhao DH, Long HL, Li M. Recent advances in carbonized non-noble metal–organic frameworks for electrochemical catalyst of oxygen reduction reaction. Rare Met. 2021;40(10):2657. https://doi.org/10.1007/s12598-020-01694-w.

[31] Wang F, Liu Y, Wei HJ, Li TF, Xiong XH, Wei SZ, Ren FZ, Volinsky AA. Recent advances and perspective in metal coordination materials-based electrode materials for potassium-ion batteries. Rare Met. 2021;40(2):448. https://doi.org/10.1007/s12598-020-01649-1.

[32] Yang J, Gao H, Ma D, Zou J, Lin Z, Kang X, Chen S. High-performance Li–Se battery cathode based on $CoSe_2$-porous carbon composites. Electrochim Acta. 2018;264:341. https://doi.org/10.1016/j.electacta.2018.01.105.

[33] Jiang J, Fan Q, Zheng Z, Kaiser MR, Chou S, Konstantinov K, Liu H, Lin L, Wang J. The dual functions of defect-rich carbon nanotubes as both conductive matrix and efficient mediator for Li–S batteries. Small. 2021;17(49):2103535. https://doi.org/10.1002/smll.202103535.

[34] Zhou X, Wang L, Yao Y, Jiang Y, Xu R, Wang H, Wu X, Yu Y. Integrating conductivity, captivity, and immobility ability into N/O dual-doped porous carbon nanocage anchored with CNT as an effective Se host for advanced K-Se battery. Adv Funct Mater. 2020;30(43):2003871. https://doi.org/10.1002/adfm.202003871.

[35] Tuinstra F, Koenig JL. Raman spectrum of graphite. J Chem Phys. 1970;53(3):1126. https://doi.org/10.1063/1.1674108.

[36] Stankovich S, Dikin DA, Piner RD, Kohlhaas KA, Kleinhammes A, Jia Y, Wu Y, Nguyen ST, Ruoff RS. Synthesis of graphene-based nanosheets via chemical reduction of exfoliated graphite oxide. Carbon. 2007;45(7):1558. https://doi.org/10.1016/j.carbon.2007.02.034.

[37] Meng YF, Liang HJ, Zhao CD, Li WH, Gu ZY, Yu MX, Zhao B, Hou XK, Wu XL. Concurrent recycling chemistry for cathode/anode in spent graphite/$LiFePO_4$ batteries: designing a unique cation/anion-co-workable dual-ion battery. J Energy Chem. 2022;64:166. https://doi.org/10.1016/j.jechem.2021.04.047.

[38] Yang CP, Xin S, Yin YX, Ye H, Zhang J, Guo YG. An advanced selenium–carbon cathode for rechargeable lithium–selenium batteries. Angew Chem Int Ed Engl. 2013;52(32):8363. https://doi.org/10.1002/anie.201303147.

[39] Park SK, Park JS, Kang YC. Selenium-infiltrated metal–organic framework-derived porous carbon nanofibers comprising interconnected bimodal pores for Li–Se batteries with high capacity and rate performance. J Mater Chem A. 2018;6(3):1028. https://doi.org/10.1039/C7TA09676C.

[40] Zeng L, Zeng W, Jiang Y, Wei X, Li W, Yang C, Zhu Y, Yu Y. A Flexible porous carbon nanofibers-selenium cathode with superior electrochemical performance for both Li–Se and Na–Se batteries. Adv Energy Mater. 2015;5(4):1401377. https://doi.org/10.1002/aenm.201401377.

[41] Du CF, Song Q, Liang Q, Zhao X, Wang J, Zhi R, Wang Y, Yu H. The passive effect of MXene on electrocatalysis: a case of $Ti_3C_2T_x$/CoNi-MOF nanosheets for oxygen evolution reaction. Chem Nano Mat. 2021;7(5):539. https://doi.org/10.1002/cnma.202100061.

[42] Yu H, Jing Y, Du CF, Wang J. Tuning the reversible chemisorption of hydroxyl ions to promote the electrocatalysis on ultrathin metal–organic framework nanosheets. J Energy Chem. 2022;65:71. https://doi.org/10.1016/j.jechem.2021.05.029.

[43] Qiu Y, Yin XJ, Wang MX, Li M, Sun X, Jiang B, Zhou H, Tang DY, Zhang Y, Fan LS, Zhang NQ. Constructed conductive $CoSe_2$ nanoarrays as efficient electrocatalyst for high-performance Li–S battery. Rare Met. 2021;40(11):3147. https://doi.org/10.1007/s12598-021-01750-z.

[44] Liu X, Wang M, Qin B, Zhang Y, Liu Z, Fan H. 2D–2D MXene/ReS_2 hybrid from $Ti_3C_2T_x$ MXene conductive layers supporting ultrathin ReS_2 nanosheets for superior sodium storage. Chem Eng J. 2022;431:133796. https://doi.org/10.1016/j.cej.2021.133796.

[45] Qiu R, Fei R, Zhang T, Liu X, Jin J, Fan H, Wang R, He B, Gong Y, Wang H. Biomass-derived, 3D interconnected N-doped carbon foam as a host matrix for Li/Na/K-selenium batteries. Electrochim Acta. 2020;356:136832. https://doi.org/10.1016/j.electacta.2020.136832.

[46] Yang X, Wang S, Yu DYW, Rogach AL. Direct conversion of metal–organic frameworks into selenium/selenide/carbon composites with high sodium storage capacity. Nano Energy. 2019;58:392. https://doi.org/10.1016/j.nanoen.2019.01.064.

[47] Luo XX, Li WH, Liang HJ, Zhang HX, Du KD, Wang XT, Liu XF, Zhang JP, Wu XL. Covalent organic framework with highly accessible carbonyls and π-cation effect for advanced potassium-ion batteries. Angew Chem Int Ed. 2022;61(10):202117661. https://doi.org/10.1002/anie.202117661.